Variational Approaches on Discontinuity Localization and Field Estimation in Sea Surface Temperature and Soil Moisture

Walter Sun, *Member, IEEE*, Müjdat Çetin, *Member, IEEE*, W. Carlisle Thacker, T. Mike Chin, and Alan S. Willsky, *Fellow, IEEE*

***Abstract*—Some applications in remote sensing require estimating a field containing a discontinuity whose exact location is *a priori* unknown. Such fields of interest include sea surface temperature in oceanography and soil moisture in hydrology. For the former, oceanic fronts form a temperature discontinuity, while in the latter sharp changes exist across the interface between soil types. To complicate the estimation process, remotely sensed measurements often exhibit regions of missing observations due to occlusions such as cloud cover. Similarly, water surface and ground-based sensors usually provide only an incomplete set of measurements. Traditional methods of interpolation and smoothing for estimating the fields from such potentially sparse measurements often blur across the discontinuities in the field.**

***Index Terms*—Curve evolution, image segmentation, image smoothing, interpolation, level sets, Mumford–Shah functional, sea surface temperature (SST), soil moisture.**

I. Introduction

SOME remote sensing problems involve estimating a field which contains discontinuities. Traditional methods of interpolation and smoothing are often used to produce estimates of such fields. Examples of such techniques include kriging [1]–[6], optimal interpolation [7]–[13], smoothing by local regression [14], and thin plate smoothing splines [15], [16]. Because these interpolation techniques do not account for discontinuities, they blur across these boundaries when estimating the field [6], [17]. To address this problem, we propose a solution based on an approach that jointly locates an unknown discontinuity and produces a smooth field estimate on either side of the discontinuity. In addition, we develop a generalization which exploits the spatial statistics of the field. In particular, we enforce and take advantage of different prior assumptions on either side of the discontinuity.

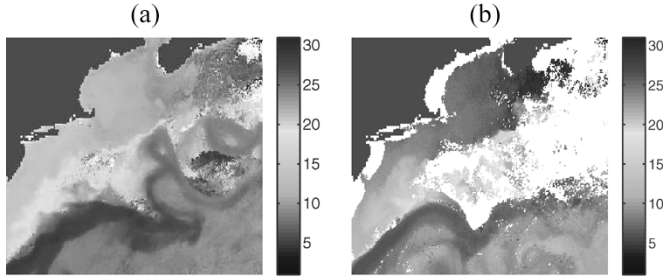

Fig. 1. Sample SST images obtained from a Geostationary Operational Environmental Satellite. The dark region in the upper left on both images is land mass, while white regions indicate missing measurements. The color bar indicates temperature in degrees Celsius. (a) Image with 2% data missing due to cloud cover. (b) A different image having 34% data missing.

One application area for our work is oceanography. In this discipline, ocean circulation [18] and, more specifically, oceanic fronts [19]–[25] have been analyzed and modeled extensively. An oceanic front, such as the Gulf Stream's north wall which separates regions of warm and cold waters in the North Atlantic, provides a strong current which results in a temperature discontinuity perpendicular to the front. Determining the location of these ocean surface features not only helps the field estimation process, but is of practical significance in itself in marine-based transportation, fishery, and oil exploration. Estimating the field on both sides of these fronts is useful to gain a better understanding of events such as coral reef bleaching [26] and global climate changes [27]. Sea surface temperature (SST) is often used to observe fronts and ocean circulation. SST can be measured by ship- or aircraft-based hydrographic surveys, or by satellite-based infrared (or microwave) sensors. While the former only offer sparse and irregular sampling patterns concentrated mostly along commercial ship lanes, the satellite measurements, which have maximum spatial resolution of approximately 5 km, are significantly attenuated by atmospheric water vapor and droplets, resulting in large data voids. These regions of missing observations are often common over oceanic regions covered by clouds over periods as long as weeks, thus making the localization of oceanic fronts a nontrivial problem [24]. For illustration, Fig. 1(a) shows an SST map for a region adjacent to the Atlantic seaboard showing the Gulf Stream's north wall when 2% of the data points in the ocean are unobserved. Fig. 1(b) shows another image with more cloud cover,

Manuscript received December 9, 2004; revised September 3, 2005. This work was supported by the National Science Foundation under ITR/AP Grant 0121182.

W. Sun was with the Laboratory for Information Decision Systems, Massachusetts Institute of Technology, Cambridge, MA 02139 USA. He is now with Microsoft Corporation, Redmond, WA 98052 USA (e-mail: waltsun@alum.mit.edu).

M. Çetin was with the Laboratory for Information Decision Systems, Massachusetts Institute of Technology, Cambridge, MA 02139 USA. He is now with the Faculty of Engineering and Natural Sciences, Sabanci University, 34956 Istanbul, Turkey.

W. C. Thacker is with the Atlantic Oceanographic and Meterological Laboratory, National Oceanic and Atmospheric Administration, Miami, FL 33149 USA.

T. M. Chin is with the Jet Propulsion Laboratory, California Institute of Technology, Pasadena, CA 91109 USA.

A. S. Willsky is with the Laboratory for Information Decision Systems, Massachusetts Institute of Technology, Cambridge, MA 02139 USA.

Digital Object Identifier 10.1109/TGRS.2005.861012

resulting in 34% data missing. Given such data, the problem is to estimate the location of the north wall as well as the underlying temperature field, interpolating over regions of missing observations.

Another application area for our techniques is hydrology. Work has been done in this area to investigate methods of estimating soil moisture fields [28], a problem in which measurements may be incomplete (e.g., due to a sparse set of ground sensors). Variations in soil moisture can significantly impact the climate and land use [29]–[33]. Hence soil moisture estimation is of interest. Different soil textures tend to have different levels of water saturation [34]–[36]. As a result, moisture fields tend to exhibit clear discontinuities at the boundary between soil types.

Kriging is commonly used to deal with missing measurements in both oceanographic and hydrological studies [37]–[40]. This method, also referred to as optimal analysis [7], [8], attempts to provide a smooth estimate of the field. The technique is similar to the update step of the Kalman filter [41], [42], where observations are incorporated in the estimation problem. Although some alternatives and variations of interpolation and smoothing have been proposed [6], [43], [44], none of the earlier methods account for discontinuities within the data. Recently, Stephenson *et al.* [17] have proposed a method that handles discontinuous spatial fields. Citing the poor performance of kriging when the field is nonstationary and the need for some method to handle fields with discontinuities, they use the Bayesian partition model of Denison *et al.* [45] to define a set of disjoint regions obtained using a Voronoi tessellation. Each region is assumed to have stationary statistics, but discontinuities are allowed across the region boundaries. One limitation of this method is that regions are constrained to be polygons. In reality, the shape of field discontinuities is not so constrained. The method we propose has the advantage of handling field estimates having a broader set of discontinuities.

Our first contribution involves applying the Mumford–Shah model [46], [47], currently used in photographic and medical imaging, to applications within oceanography and hydrology. In this framework, we formulate the problem of joint boundary localization and field estimation as an optimization problem. The resulting objective functional contains terms that impose data fidelity, as well as indicate a preference for relatively smooth boundaries and smooth fields on either side of the boundary. From an estimation-theoretic standpoint, the preference for smooth fields can be viewed as a specific prior on the first- and second-order statistics of the field. The optimization problem is solved numerically using a coordinate descent strategy and active contour methods [48], [49].

Next, motivated by the desire to incorporate different types of first- and second-order statistics on either side of a discontinuity, we propose a generalization of the Mumford–Shah functional, which we henceforth call the modified Mumford–Shah (MMS) functional. The MMS functional allows for more general priors based on the statistics of the regions, which is particularly useful when the statistics are spatially varying within each region. For example, in the oceanographic application, the underlying SST field is known *a priori* to be colder as we move north of the Gulf Stream's north wall and warmer as we move south. We show that by simply providing a prior mean which is a piecewise linear function of the distance from the temperature discontinuity, we obtain a better estimate of sea surface temperatures and of the discontinuity. Development of the MMS functional constitutes our second contribution.

In Section II, we introduce the technique of active contours, a method which we incorporate in our algorithm to solve our optimization problem. In Section III, we describe the Mumford–Shah functional, explaining how it locates a discontinuity and estimates a field without smoothing across the boundary. In Section IV, we propose the MMS functional and explain how this may be more appropriate when specific spatial statistics are known. In Section V, we present experiments on synthetic and real SST measurements, as well as simulated soil moisture data. Using these experiments, we compare the results of our techniques against three existing methods of interpolation and smoothing. Section VI summarizes the paper and discusses possible extensions of this work.

II. Active Contour Methods

Active contours [48]–[54] are curves which evolve to minimize an associated objective functional that incorporates constraints from available data (e.g., imagery). The goal of this technique is to obtain a segmentation (i.e., locate a boundary) in the spatial field or image of interest. Mathematically, this amounts to determining

$$\hat{C} = \underset{\vec{C}}{\operatorname{argmin}}[E(\vec{C})]$$

where $\hat{C}$ represents the segmentation and E is the energy functional to be minimized (on which we will have more to say in subsequent sections). If we introduce an iteration time parameter t, we may evolve our curve according to a differential equation of the form

$$\frac{\partial \vec{C}}{\partial t} = -\mathcal{F}(\vec{C}) \tag{1}$$

where $\mathcal{F}(\vec{C})$ is a force functional. Choosing $\mathcal{F}(\vec{C})$ as the first variation of $E(\vec{C})$ allows the curve to move in the direction of steepest descent. The curve is evolved until steady-state is reached (i.e., $\mathcal{F}(\vec{C}) = 0$).

The evolution of such a contour can be performed in a variety of ways. One standard approach involves discretizing the curve into a set of marker points that are moved from iteration to iteration [48], [55]. At each iteration, a curve can be constructed by some method of interpolation. Kass [48] parameterizes an initial curve and moves individual marker points to evolve the curve. The evolving curves in such approaches are commonly referred to as "snakes." This technique has several drawbacks [56], [57]. First, nothing in the equations of motion prevent the discretized points from moving together, leaving an unevenly discretized curve. Second, stable evolution requires a very small time-step. Third, marker points cannot easily handle changes in topology of the evolving curve. Some modifications may help to remedy these problems, such as more frequent resampling of the points on the curve to redistribute them evenly. However, the added complexity leads many to consider alternate methods. One such technique, which we use for our curve evolution, involves level set methods. Level set methods, developed by Osher and Sethian [58], [59], provide a robust way of evolving a contour because they handle topological changes seamlessly and do not require

labels or marker points. Instead of evolving discretized points on the curve, level set methods evolve a surface whose zero level set represents the curve.

Obviously the choice of the functional $E(\vec{C})$ greatly impacts the nature of the curve or level set evolution equation and the resulting segmentation obtained through minimization. In the following sections, we describe two different functionals that we use to solve our estimation problem.

III. Mumford–Shah Functional

To accomplish joint field estimation and boundary localization simultaneously, we describe a functional which depends on both the boundary and the field on either side of the boundary. In this formulation, the minimized functional yields a localization of the boundary (e.g., an oceanic front) and a field estimate (e.g., sea surface temperature) simultaneously. The Mumford–Shah functional [46], [47], also referred to as a weak membrane model by Blake and Zisserman [60], is one example of a functional dependent on both the curve location and field values.

Mathematically, the Mumford–Shah functional is a three-term energy functional defined by

$$E_{\mathrm{MS}}(f,\vec{C}) \equiv \alpha \int_{U} \left(f(\mathbf{x}) - g(\mathbf{x})\right)^2 d\mathbf{x} + \beta \int_{\Omega\setminus\vec{C}} |\nabla f(\mathbf{x})|^2 \, d\mathbf{x} + \gamma \oint_{\vec{C}} ds \quad (2)$$

where Ω is the overall two-dimensional spatial region of interest, U is the subset of Ω where data are available, $\mathbf{x}$ represents a two-dimensional position vector, s denotes the arc length, f is the unknown field to be estimated, $\vec{C}$ is the unknown boundary to be estimated, g is the observed data, and α, β, and γ are nonnegative tunable parameters. The parameters provide two degrees of freedom (the choice of f and $\vec{C}$ is invariant to scale, so the two independent parameters could be α/γ and β/γ) for the user to vary depending upon which terms one wants to place higher confidence. This freedom may be desirable in adapting the technique to particular applications and tasks, as a user can tune the parameters as needed on a few test cases before using these values on a larger set of examples.

The specific choice of parameters is context-dependent (e.g., for our applications, it depends on the magnitude of observation noise, the typical length of the boundaries in the field, and the degree of smoothness of the field). Moreover, the automatic choice of parameters is an open problem and beyond the scope of this paper. However, it has been a subject of much previous work in other applications where similar variational techniques are used [61]–[67]. The methods described in these works, such as ordinary and generalized cross-validation [61]–[64], the L-curve method [65], [66], and the discrepancy principle [66], [67], are different algorithms used to determine a set of parameters. These methods have been used for parameter selection in variational techniques applied to problems in computer vision [48]–[50], [53], [54], [60], [68]–[71] and can be applied similarly to earth science applications within the framework we propose in this paper.

A goal of the paper is to introduce a robust joint boundary and field estimation framework for geoscience problems, allowing users the flexibility to choose parameters as appropriate based on the application. The functionals we introduce have parameters that can be determined by one of the methods cited above or by other ad hoc approaches that may suit a particular problem.

In our applications, f represents the sea surface temperature or soil moisture, while $\vec{C}$ represents the location of the discontinuity in the field, representing the oceanic fronts or the interface between soil types. The first term in the functional is known as the data fidelity term. This term penalizes deviations of the estimated field from the observed data. The second term penalizes the gradient of the field everywhere except across the boundary, thus enforcing smooth fields on either side of the boundary while not penalizing a potentially sharp discontinuity across the boundary. Finally, the third term penalizes curve length. Without this term, $E_{\mathrm{MS}}(f,\vec{C})$ can be minimized to zero by having boundaries everywhere, which is not a useful solution. The addition of this regularization term helps to capture the physical characteristic of producing smooth, rather than jagged estimates of oceanic fronts and soil boundaries.

We minimize a discretized version of $E_{\mathrm{MS}}(f,\vec{C})$ to obtain the field and boundary estimate. The discretization, which involves sampling the continuous region Ω on an equally spaced spatial grid, yields

$$E_{\mathrm{MS}}\left(\begin{bmatrix}\mathbf{f}_{R_1}\\ \mathbf{f}_{R_2}\end{bmatrix},\vec{C}\right) = \alpha\left[\|H_{R_1}\mathbf{f}_{R_1}-\mathbf{g}_{R_1}\|_2^2+\|H_{R_2}\mathbf{f}_{R_2}-\mathbf{g}_{R_2}\|_2^2\right] + \beta\left[\mathbf{f}_{R_1}^T L^T L\mathbf{f}_{R_1} + \mathbf{f}_{R_2}^T L^T L\mathbf{f}_{R_2}\right] + \gamma l(\vec{C}) \quad (3)$$

where the matrix L is the discrete representation of the gradient operator, R_1 and R_2 are the regions on either side of the boundary, $\mathbf{g}_{R_1}$ and $\mathbf{g}_{R_2}$ are observations lexicographically unwrapped and written in vector form, $\mathbf{f}_{R_1}$ and $\mathbf{f}_{R_2}$ are similarly unwrapped vectors, and $l(\vec{C})$ represents the length of $\vec{C}$. In (3), H_{R_i} associates $\mathbf{f}_{R_i}$ with the associated observation $\mathbf{g}_{R_i}$ (i.e., if the mth observation in $\mathbf{g}$ corresponds to a measurement of the nth element of $\mathbf{f}_{R_i}$, then $H_{R_i}(m,n)=1$, and it is only these entries of H_{R_i} that are nonzero). So, $\|H_{R_i}\mathbf{f}_{R_i}-\mathbf{g}_{R_i}\|_2^2$ represents the sum of squares of the differences between observed samples $\mathbf{g}_{R_i}(\mathbf{x})$ and the corresponding field estimate $\mathbf{f}_{R_i}(\mathbf{x})$, where $\mathbf{x}$ denotes the spatial locations where we have observations.

Minimizing the Mumford–Shah functional produces a piecewise smooth field estimate. Tsai *et al.* [69] and Chan and Vese [70] describe active contour implementations which minimize the Mumford–Shah functional. Other related formulations have been introduced which also address the issue of simultaneous boundary and field estimation. Functionals proposed by Chan and Vese [70] and Yezzi *et al.* [71] apply the more restrictive assumption of a spatially constant field estimate on either side of the boundary.

When viewed as solving a maximum *a posteriori* (MAP) estimation problem, Mumford–Shah enforces a Gaussian prior on each region, with an inverse covariance, or information matrix, of $(L^T L)$ [from (3)] and a spatially constant mean. Hence, Mumford–Shah provides one particular prior on the field. Motivated to use different priors on the field (e.g., those more appropriate for our target applications), we propose a generalization of Mumford–Shah, which we describe in the next section.

IV. Modified Mumford–Shah Formulation

In the Mumford–Shah formulation shown in (3), the terms containing L impose a particular prior covariance and a spatially constant mean. Sometimes, a more accurate, yet still simple, prior model may be available. For instance, sea surface temperatures have spatially varying means. More specifically, we expect temperatures north (south) of the Gulf Stream's north wall to decrease (increase) as a function of the distance from this discontinuity. Furthermore, an information matrix different from the $L^T L$ of (3) may provide a better characterization of the second-order statistics within the regions. In this section, we propose a generalization of the Mumford–Shah functional which incorporates general first- and second-order statistics of the field on either side of the discontinuity.

We note that the modified Mumford–Shah approach we discuss in this section and Mumford–Shah work well if the true field and boundary fit the underlying model. Namely, in these approaches, we assume; 1) a measurement model which has additive Gaussian noise; 2) piecewise smooth fields (this actually does not need to be a limitation if we do not require that $\mathcal{D}$ be a derivative operator); and 3) smooth curves for the boundary. If the desired field is not smooth, the boundary is expected to be jagged, or the measurement model is not Gaussian, then we do not expect good results using these two approaches. However, we find that smoothness assumptions (on the field and boundary) are reasonable in a variety of applications, such as the ones we examine in the experiments.

A. Energy Functional

We first introduce the MMS functional in continuous form

$$\begin{aligned} E_{\mathrm{MMS}}(f,\vec{C}) = {} & \alpha \int\limits_{U\cap R_1} \left(f(\mathbf{x})-g(\mathbf{x})\right)^2 d\mathbf{x} \\ & + \alpha \int\limits_{U\cap R_2} \left(f(\mathbf{x})-g(\mathbf{x})\right)^2 d\mathbf{x} \\ & + \beta \int\limits_{R_1}\int\limits_{R_1} \mathcal{D}\left[f(\mathbf{x})-\mu_{R_1}(\mathbf{x})\right] b_{R_1}(\mathbf{x},\mathbf{z}) \\ & \times \mathcal{D}\left[f(\mathbf{z})-\mu_{R_1}(\mathbf{z})\right] d\mathbf{x}d\mathbf{z} \\ & + \beta \int\limits_{R_2}\int\limits_{R_2} \mathcal{D}\left[f(\mathbf{x})-\mu_{R_2}(\mathbf{x})\right] b_{R_2}(\mathbf{x},\mathbf{z}) \\ & \times \mathcal{D}\left[f(\mathbf{z})-\mu_{R_2}(\mathbf{z})\right] d\mathbf{x}d\mathbf{z} + \gamma \oint\limits_{\vec{C}} ds. \end{aligned} \quad (4)$$

In this equation, $\mathcal{D}$ is an arbitrary linear differential operator (where the higher the order of the derivatives, the more smooth the field estimate), $\mu_{R_1}(\mathbf{x})$ and $\mu_{R_2}(\mathbf{x})$ are spatially varying mean functions in the respective regions. In particular, we model the means as functions of the distance from the boundary. So, $\mu_{R_i}(\mathbf{x}) = \phi_i(d(\mathbf{x},\vec{C}))$, where $d(\mathbf{x},\vec{C})$ is the distance of point $\mathbf{x}$ to $\vec{C}$, and ϕ_i can be an arbitrary function (e.g., when we apply this to SST data, we choose $\phi_i(z) = \eta + \rho z$, an affine function, where η and ρ are determined from historical data). The function $b_{R_i}(\mathbf{x},\mathbf{z})$ allows for a more general dependency between points within the same region than Mumford–Shah does.[1]

[1]Note that b must be a positive semidefinite function.

The data fidelity and curve length terms of the MMS functional are the same as those in Mumford–Shah. However, we replace the second term in (2) with terms which incorporate the prior means μ_{R_1} and μ_{R_2} and an arbitrary linear differential operator $\mathcal{D}$ on the field f. For perspective, this functional reduces to the Mumford–Shah functional in the special case where the means are zero, the $\mathcal{D}$ operator is the gradient operator, and b is the Dirac delta function. Various possibilities for the priors exist (e.g., historical data can be used to estimate the mean and covariance) [72]–[76]. In our examples, we make specific choices for these parameters to illustrate the characteristics and advantages of this approach. The MMS functional yields improved results over Mumford–Shah whenever we can accurately capture the spatial variability through the appropriate selection of $\mathcal{D}$, μ_{R_i}, and b_{R_i}. We now describe how (4) is minimized numerically using coordinate descent.

B. Numerical Solution

Ideally, we wish to solve for f and $\vec{C}$ simultaneously. However, given that the gradient of $E_{\mathrm{MMS}}(f,\vec{C})$ is not easily attainable, we approach the solution to this problem using the technique of coordinate descent. This method is an iterative approach in which at each step, all but one of the varying parameters is held fixed, while the remaining parameter is updated in a manner which decreases the functional. Within each iteration, each of the parameters is updated exactly once.

Using this technique, we divide each iteration into two main steps. First, having $\vec{C}$ fixed, we compute the value of f which minimizes $E_{\mathrm{MMS}}(f,\vec{C})$ for the particular value of $\vec{C}$.[2] Then, with f fixed, we evolve $\vec{C}$ in the direction of the first variation of $E_{\mathrm{MMS}}(f,\vec{C})$ with respect to $\vec{C}$. For this curve evolution step, we ideally want both b and μ to vary with the curve, since both can in general be functions of $\vec{C}$. However, for computational simplicity, we hold b and μ fixed as we evolve $\vec{C}$ and then recompute b and μ to accurately reflect the new position of $\vec{C}$ before the next iteration. The use of this approximation does not appear to adversely affect the convergence to a solution. The iterative process is repeated until we converge to an equilibrium. The method of coordinate descent does not guarantee convergence to the global minimum, but given a reasonable choice of initialization, our algorithm appears to converge to a sufficiently good solution as seen from the experiments in Section V. The full derivation of the numerical solution may be found in Appendix I.

V. Experimental Results

We perform experiments on SST data and soil moisture maps. We demonstrate the advantage of using our simultaneous boundary detection and field estimation method by comparing results from Mumford–Shah and MMS to existing techniques of kriging, gradient smoothing, and smoothing splines. These existing methods fundamentally have no provision to handle the presence of discontinuities. The illustrations from our results show how the failure to handle discontinuities leads to blurring across the boundaries. In the first example involving soil moisture, we demonstrate how Mumford–Shah and MMS do better

[2]One could take a gradient step in the direction which decreases the functional rather than find the minimum and still attain a solution [57], but we actually solve for the minimizing f in each step.

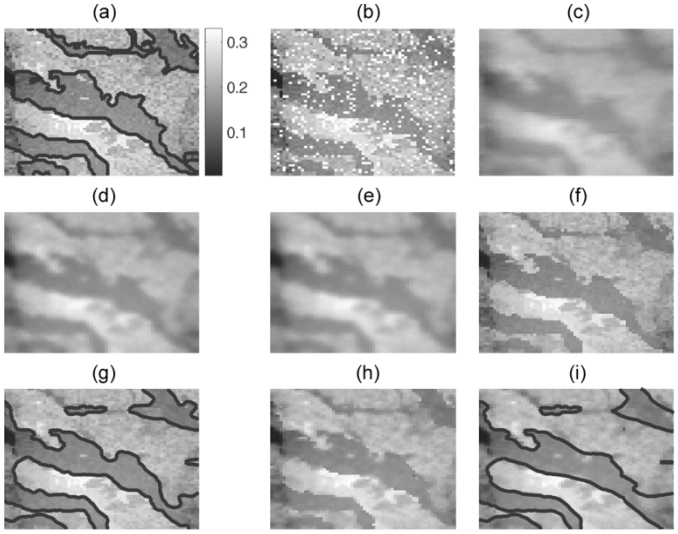

Fig. 2. Estimation of soil moisture in an example where 90% of the data are observed. Images show fractional volume of water in the soil. (a) The original soil moisture map with color bar (color bar valid for all images) and true boundary overlaid. (b) The observed data. (c) Estimate using kriging. (d) Estimate using gradient smoothing. (e) Estimate using smoothing splines with second-order derivatives. (f) Field estimate using Mumford–Shah. (g) Field and boundary estimates using Mumford–Shah. (h) Field estimate using MMS. (i) Field and boundary estimates using MMS.

than other interpolation techniques.[3] In the second example involving SST maps, we show how MMS can exploit spatially varying statistics to yield better results than Mumford–Shah, which in turn provides better results than the other interpolation methods. Before presenting the results, we note that the tunable parameters α, β, and γ in (2) and (4) have been subjectively chosen to provide reasonable results. Similarly, the choices of parameters for the methods we compare against, namely kriging, gradient smoothing, and smoothing splines, have been made with an attempt to provide as good results as possible.

A. Simulated Soil Moisure Data

We examine soil moisture measurements generated from a simulation (more samples of this simulation can be found in [77]) based on the Community Land Model (CLM), a model designed at the National Center for Atmospheric Research (NCAR) [78]. The CLM produces variable soil moisture in a spatial domain having different soil types. While the data used originated from a simulation, we note that when raw data are collected from passive instruments, brightness temperature is generally recorded. To convert this data to soil moisture, a radiative transfer model is often used [79].

The particular simulation we consider assumes a uniform spatial distribution of rainfall. After time elapses from a period of rainfall, the surface soil moisture of the sand region tends to be much drier than any of the other soil types present. As a result, we pose the problem of segmenting the boundary (at a given time after a recent rainfall) between two regions, the first containing sand and the second containing other soil types, as well as estimating the soil moisture in each of these regions. Fig. 2(a) shows an example of a soil moisture map with the boundary (given from the simulation) separating the sand region from the other soil types.

[3]Because we assume mean-statistics are not spatially varying, we expect Mumford–Shah and MMS to yield similar results for this example.

TABLE I
STANDARD ERROR PER PIXEL BETWEEN THE FIELD ESTIMATES AND A SMOOTHED VERSION OF THE SIMULATED OBSERVATION. NOTE THAT THE VARIATIONAL METHODS WE PROPOSE HAVE SMALLER ERRORS

	Kriging	Gradient Smoothing	Smoothing Splines	Mumford-Shah Functional	MMS Functional
90% observed	0.0299	0.0231	0.0240	0.0183	0.0186
81% observed	0.0328	0.0269	0.0274	0.0224	0.0256

For the field estimates, the particular simulation we use is at a much finer spatial scale than the field information we want to capture. Hence, the simulation essentially provides a *noisy version* of the coarser scale soil moisture field we are interested in estimating. Thus, to evaluate field estimation accuracy, we compare the resulting estimates with a coarser scale version of the simulations obtained using gradient smoothing as shown in (5) within each of the regions (assuming that the boundary is known).

For the MMS method, we compute the mean moisture for sand and that for the other region from simulated data and use these as values for μ_{R_1} and μ_{R_2} in (4), respectively. For this application, the means are chosen to be spatially nonvarying because at this scale, no systematic variability can be discerned from the mean field. We choose $\mathcal{D}$ to be the second derivative operator and b to be the Dirac delta function. The choice of a second derivative operator for $\mathcal{D}$ means we enforce an even greater amount of smoothness than that obtained in Mumford–Shah, which uses a first derivative operator.

To provide perspective for how well the estimation methods which explicitly consider boundaries perform, we compare the estimation of the field using Mumford–Shah and MMS with a few standard methods of interpolation and smoothing. In particular, we consider kriging [1], [3], [6],[4] gradient smoothing [16], and a second-order smoothing spline [15]. In essence, gradient smoothing involves applying Mumford–Shah without any notion of a boundary. Mathematically, the gradient smoothing method minimizes

$$E_{\mathrm{GS}}(f)=\alpha\int_U (f(\mathbf{x})-g(\mathbf{x}))^2\,d\mathbf{x}+\beta\int_\Omega |\nabla f(\mathbf{x})|^2\,d\mathbf{x} \quad (5)$$

where the variables are as defined previously. Similarly, the second-order smoothing spline minimizes

$$E_{\mathrm{SS}}(f)=\alpha\int_U (f(\mathbf{x})-g(\mathbf{x}))^2\,d\mathbf{x} +\beta\int_\Omega \left[\left(\frac{\partial^2 f}{\partial x^2}\right)^2+\left(\frac{\partial^2 f}{\partial y^2}\right)^2+2\left(\frac{\partial^2 f}{\partial x\partial y}\right)^2\right]d\mathbf{x} \quad (6)$$

as set forth in Wahba and Wendelberger [15] (where $\mathbf{x}\equiv(x,y)$). This method is similar to MMS for the choice of $\mathcal{D}$ and b mentioned above except that it ignores the possible presence of boundaries.

[4]The kriging results were obtained using ordinary kriging with nugget effect using a 5×5 window of neighbors for prediction. Other methods of kriging can be considered. See the MATLAB Kriging Toolbox (http://globec.whoi.edu/software/kriging/V3/intro_v3.html) for different options.

We consider three examples having different coverages of observed data. For the first example, we consider the case where 90% of the region is observed [Fig. 2(b)]. Fig. 2(c) shows the interpolation resulting from kriging, Fig. 2(d) illustrates the estimate from gradient smoothing, and Fig. 2(e) shows the result from second-order smoothing splines. In these three cases, some of the measurement noise, apparent from Fig. 2(a), is removed, but the discontinuities are slightly blurred.

Fig. 2(f) shows the field estimate using Mumford–Shah, while Fig. 2(g) shows the same estimate with the boundary overlaid (for reference). Similarly, Fig. 2(h) shows the field estimate using MMS, while Fig. 2(i) shows the estimate with the boundary overlaid. A binary threshold was used to determine the initial boundary for the active contour evolution. These results illustrate that Mumford–Shah and MMS can locate the boundary and produce field estimates that maintain a sharp transition at the region boundaries. In addition, we note that through the use of level set methods [58], [59] for our curve evolution, we are able to detect boundaries which are not simple closed curves, as shown in Fig. 2(g) and (i). Quantitatively, Table I shows the standard error per pixel for the variational techniques as well as the traditional methods. From these results, it can be seen that the errors from the variational techniques we propose are smaller than those from the traditional methods.

To compare the accuracy of the boundary localization, we first need to find a way to generate a boundary from the field estimates of the traditional approaches. A direct approach involves using adaptive binary thresholding, where for each instance, we find the threshold which most closely matches the ground truth according to a normalized symmetric difference (NSD) measure, which we define as

$$\mathrm{NSD}(R_1, R_2) = \frac{A(R_1 \cap \bar{R}_2) + A(\bar{R}_1 \cap R_2)}{A(R_1 \cup R_2)} \qquad (7)$$

where $\bar{R}_i$ represents the complement of region R_i and $A(R_i)$ is the area of region R_i. After boundary localization through such manual adaptive processing, we quantify the closeness of the resulting boundary to the truth by computing NSD. This process is in practice unrealizable since we do not necessarily have ground truth. Thus, the boundaries from the traditional approaches are actually the best case results that can come from these methods. We also use the same measure for the boundaries generated by our proposed techniques. For the boundaries shown in Fig. 3, the NSD for the boundary determined using kriging is 0.3469, that for gradient smoothing is 0.4158, and that for second-order smoothing splines is 0.4105. In contrast, the NSD for Mumford–Shah is 0.1502, while that for MMS is 0.1789. Hence, our proposed methods do better in finding boundaries than the traditional approaches. Note that for the soil moisture examples, we do not expect MMS to necessarily outperform Mumford–Shah because the fields are assumed to have spatially constant means (unlike the SST example described in the next section).

For the second example, we consider the situation where a large rectangular region is unobserved, as shown in Fig. 4(b) [compare with the full observation in Fig. 4(a)]. This may simulate a scenario where blocks of measurements are locally obtained by regional stations, but because of a gap in the spatial coverage of the stations, certain areas are unobserved. Again, Fig. 4(c)–(e) shows interpolations using kriging, gradient smoothing, and second-order smoothing splines, respectively. In all three images, we observe a smooth estimate in the missing rectangular region as well as a smoothing of the observed data. Furthermore, as expected, the discontinuity at the soil boundary is not well-defined in the missing region for any of these three field estimates.

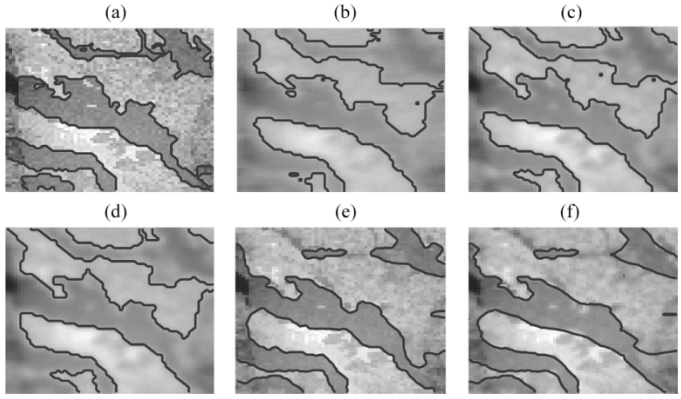

Fig. 3. Estimates of the boundary between soil types given the observation shown in Fig. 2. (a) The original soil moisture map with true boundary shown. (b) Estimate using kriging. (c) Estimate using gradient smoothing. (d) Estimate using smoothing splines. (e) Estimate using Mumford–Shah. (f) Estimate using MMS.

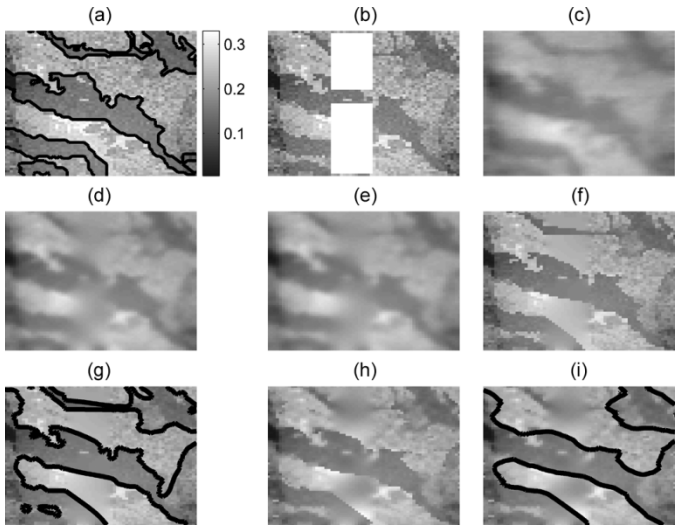

Fig. 4. Estimation of soil moisture. Images show fractional volume of water in the soil. (a) The original soil moisture map. (b) The observed data, a moisture map with a rectangular region unobserved (representing 81% observed data). (c) Estimate using kriging. (d) Estimate using gradient smoothing. (e) Estimate using smoothing splines with second-order derivatives. (f) Field estimate using Mumford–Shah. (g) Field and boundary estimates using Mumford–Shah. (h) Field estimate using MMS. (i) Field and boundary estimates using MMS.

Fig. 4(f) shows the field estimate using Mumford–Shah with the boundary localization overlaid in Fig. 4(g), while Fig. 4(h) and (i) shows the same using the MMS functional. As the initialization for the curve evolution of Mumford–Shah and MMS, we again use a threshold of the moisture data where there are observations. Across the unobserved block, we linearly interpolate the thresholded boundary. The results from Mumford–Shah and MMS preserve the boundary between the two soil types, which lead to more accurate field estimates. In particular, Fig. 4(f) and (h) does not exhibit blurring across the soil boundaries, which is the case in Fig. 4(c)–(e). Table I summarizes the results, confirming that our proposed methods yield smaller error than the traditional approaches.

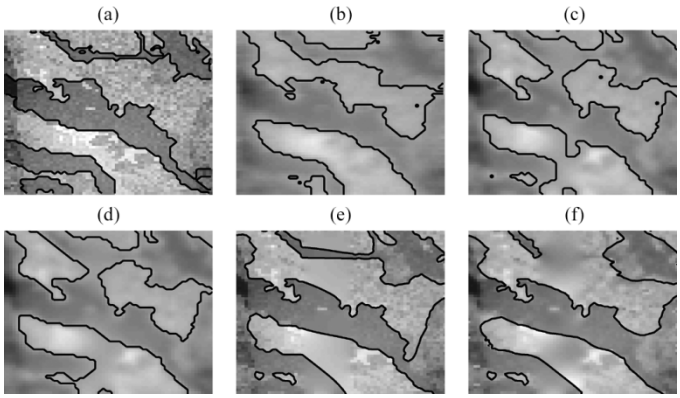

Fig. 5. Estimates of the boundary between soil types given the observation shown in Fig. 4. (a) The original soil moisture map with true boundary shown. (b) Estimate using kriging. (c) Estimate using gradient smoothing. (d) Estimate using smoothing splines. (e) Estimate using Mumford–Shah. (f) Estimate using MMS.

TABLE II
NORMALIZED SYMMETRIC DIFFERENCE BETWEEN TRUE BOUNDARY AND ESTIMATED BOUNDARY. FOR THE 90% OBSERVED EXAMPLE, WE SEE THAT MUMFORD-SHAH AND MMS DO MUCH BETTER THAN THE TRADITIONAL METHODS WHILE FOR 81% OBSERVED, THESE TWO METHODS DO SLIGHTLY BETTER

	Kriging	Gradient Smoothing	Smoothing Splines	Mumford-Shah Functional	MMS Functional
90% observed	0.3469	0.4158	0.4105	0.1502	0.1789
81% observed	0.4327	0.3519	0.3569	0.2909	0.3469

Again, we evaluate the boundaries using binary thresholding. For the boundaries shown in Fig. 5, the NSD for the boundary determined using kriging is 0.4327, that for gradient smoothing is 0.3519, and 0.3569 for second-order smoothing splines. In contrast, the NSD for Mumford–Shah is 0.2909, while that for MMS is 0.3469. Table II summarizes the results of the boundary estimates for these two examples.

In our third example, we simulate the situation where we have a sparse set of sensors to collect measurements. In particular, suppose our observations are 11% of the spatial field of interest, as shown in Fig. 6(b). Fig. 6(c) shows the result using kriging, Fig. 6(d) shows the field estimate using gradient smoothing, while Fig. 6(e) illustrates the result using second-order smoothing splines. As one would expect, each of these three methods smoothes the region between the sparse set of observations.

Now, given the measurements alone, it would be difficult to find a reasonable initialization for the curve evolution methods (Mumford–Shah and MMS). So suppose that we have some knowledge of the boundary, either from a segmentation of the same spatial domain at a previous time in the current observation sequence or from an ensemble of historical data. In our experiments, we take the segmentation from a different simulation of this region and use this as the initialization. With this as a starting point, we show that we can provide a reasonable estimate for the boundary location as well as a field estimate of the spatial domain that appears more accurate than the conventional methods shown in Fig. 6(c)–(e).

Fig. 6(f) shows the result using Mumford–Shah [boundary shown in Fig. 6(g)], while Fig. 6(h) and (i) illustrates the same

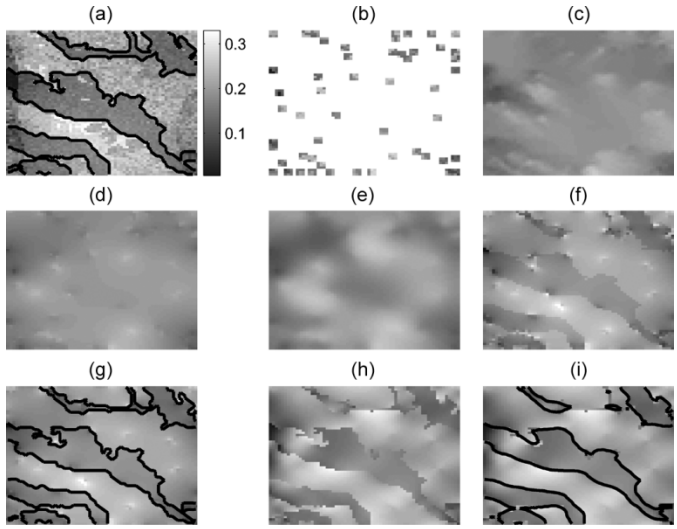

Fig. 6. Estimation of soil moisture where only a sparse set of measurements are made. Images show fractional volume of water in the soil. (a) The original soil moisture map with color bar (color bar valid for all images in this figure). (b) Observed data representing 11% of the entire spatial field. (c) Estimate using kriging. (d) Estimate using gradient smoothing. (e) Estimate using smoothing splines with second-order derivatives. (f) Field estimate using Mumford–Shah. (g) Field and boundary estimates using Mumford–Shah. (h) Field estimate using MMS. (i) Field and boundary estimates using MMS.

using MMS. In Mumford–Shah and MMS, the field is smoothed within each region, but the discontinuity is preserved. Furthermore, finding the optimal field for each region separately provides a more accurate moisture estimate for both regions.

Given a sparse dataset such as this example, localization of the boundary would be difficult without a good initialization. However, the purpose of this example is to illustrate that, by incorporating any available prior information, our method uses this knowledge to provide an improved boundary estimate based on the measurements as well as a reasonable estimate of the field.

Before we conclude this discussion on soil moisture data, we discuss the computational complexity of each of the methods analyzed. The following computation times are obtained using a desktop personal computer having a Xeon 2.2-GHz processor running MATLAB version 6.5 on a Linux OS. The computed times are based on the time required to produce a field estimate of the soil moisture maps as shown in Fig. 4. The soil moisture field consists of a 64×64 grid of pixels. Kriging requires 8.56 s to produce the field estimate, while gradient smoothing takes 1.75 s. Iterating Mumford–Shah for 100 steps (an approximate time for convergence) requires 20.53 s.

Mumford–Shah uses first derivatives for interpolation in a manner similar to that in gradient smoothing. Although Mumford–Shah has greater computational complexity, it provides an improved field estimate over gradient smoothing. Furthermore, Mumford–Shah performs the additional task of localizing the boundary. To provide a similar comparison with second-order smoothing splines, we choose the second derivative operator for $\mathcal{D}$ in MMS for our analysis. Second-order smoothing splines requires 10.73 s, while the computation time for MMS for this choice of $\mathcal{D}$ is 32.98 s for 100 iterations. MMS results in somewhat higher computational complexity than second-order smoothing splines. However, in return it

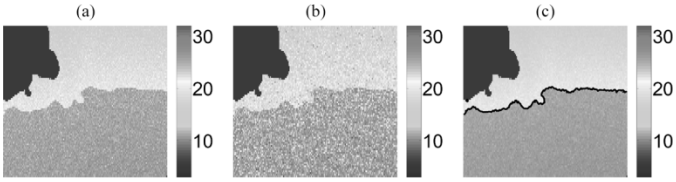

Fig. 7. Boundary and field estimation of synthetic SST field (temperatures in degrees Celsius). (a) The original synthetic field to be estimated (dark mass at top left is land). (b) Simulated measurements containing additive IID noise. (c) Field estimate using MMS with boundary overlaid. Note that this estimate removes some of the IID measurement noise.

provides an improved field estimate as well as boundary localization.

B. Sea Surface Temperature Data

In soil moisture estimation, because each soil type has a mean that does not vary systematically, Mumford–Shah and MMS yield similar results. However, in the oceanographic application we consider here, it is known that sea surface temperatures vary spatially in a systematic manner. In the following analysis of SST measurements, we show that in an application with spatially varying fields, MMS provides better estimates than Mumford–Shah.

1) Synthetic SST Data: We initially analyze a synthetic data sequence designed to simulate a region in the North Atlantic. First, we define a temperature discontinuity characteristic of an oceanic front. From this, a spatially varying mean temperature map is generated using the following assumptions: 1) south of the discontinuity, the mean temperature is $\phi_1(d(\mathbf{x},\vec{C})) = 25 + 0.002d(\mathbf{x},\vec{C})$ degrees Celsius, where $d(\mathbf{x},\vec{C})$ is the distance in kilometers of the point $\mathbf{x}$ from the front $\vec{C}$ and 2) north of the discontinuity, the mean temperature is $\phi_2(d(\mathbf{x},\vec{C})) = 20 - 0.01d(\mathbf{x},\vec{C})$ degrees Celsius. We use a linear temperature model because we assume that we are operating in the linear portion of a particular temperature model $T = T_0\cos(\sin(\theta))$, where θ is degrees latitude and T_0 is the equatorial temperature. This model is obtained as an approximation of surface temperature based on a one-dimensional energy balance model of climate [80], [81]. Next, we define a Gaussian covariance matrix for each region to enforce correlation between nearby points. In particular, we choose $K[\mathbf{x},\mathbf{z}] = \exp[-0.02d^2(\mathbf{x},\mathbf{z})]$ (where $d(\mathbf{x},\mathbf{z})$ is the distance in kilometers between $\mathbf{x}$ and $\mathbf{z}$) for points $\mathbf{x}$ and $\mathbf{z}$ on the same side of the boundary.[5] Using these assumptions, our synthetic temperature map is generated and shown in Fig. 7(a). Finally, independent, identically distributed pixelwise white noise with zero mean and standard deviation of two is added to simulate measurement noise. Fig. 7(b) shows such synthetically generated measurements.

First, we apply the MMS functional to the dataset shown in Fig. 7(b). Again, we make the assumption that b in (4) is the Dirac delta function. However, instead of choosing the differential operator $\mathcal{D}$, we assume we know the true covariance K (given b, this choice of K implicitly determines the choice of $\mathcal{D}$). The results of the field estimation are shown in Fig. 7(c), with the estimated boundary overlaid. From this image, we observe that the MMS method localizes the boundary and substantially reduces the noise in the field (quantitatively, the reduction in standard error is 26%).

[5]The multiplicative constant 0.02 in the exponential was chosen so that there would be some dependencies beyond just the neighboring pixels, but it had to be chosen carefully to ensure that K was a mathematically valid covariance [82].

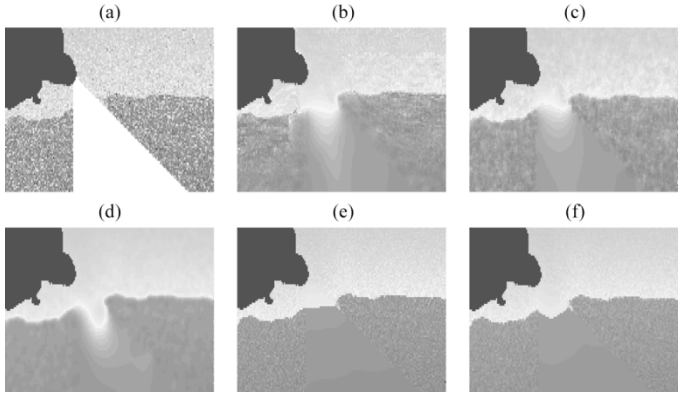

Fig. 8. Boundary and field estimation of synthetic SST field. (a) The measurement data are as in Fig. 7(b), except that a triangular region is unobserved. (b) Field estimate using kriging. (c) Field estimate using gradient smoothing. (d) Field estimate using second-order smoothing splines. (e) Field and boundary estimate using the Mumford–Shah functional. Note that the boundary is a straight line across the region of missing observations. (f) Field and boundary estimate using the MMS functional.

TABLE III
STANDARD ERROR IN THE INTERPOLATED TRIANGULAR REGION AND ENTIRE IMAGE AS SHOWN IN FIG. 8

Std Err (deg Celsius)	Kriging	Gradient Smoothing	Smoothing Splines	Mumford-Shah Functional	MMS Functional
Missing Triangle	2.41	1.42	1.71	1.36	1.15
Entire Image	1.84	1.14	1.19	0.76	0.73

Satellite measurements have unobserved regions due to a combination of cloud cover and the limited range of the satellite's swath. Motivated by this fact, we generate an example where a spatial field is not fully observed by using the previous simulation of Fig. 7 and assuming that a large triangular region is unobserved. This is shown in Fig. 8(a), where the area with no measurements is shown in white. As with the soil moisture examples, we compare the joint boundary and field estimation techniques with three traditional methods of interpolation. In particular, we apply kriging [Fig. 8(b)], gradient smoothing [Fig. 8(c)], and second-order smoothing splines [Fig. 8(d)] to the observation shown in Fig. 8(a). In comparison with the true field in Fig. 7(a), we observe that the field estimates using kriging, gradient smoothing, and smoothing splines do not accurately preserve the boundary in the unobserved region.

Fig. 8(e) shows the result using the Mumford–Shah functional from (2), while Fig. 8(f) shows the outcome using the MMS functional proposed in (8). For the latter, $\mathbf{m}_{R_i}$ and $K_{R_i}^{-1}$ are the mean and covariance statistics, respectively, used in the simulation shown in Fig. 7(a). Note that in the regions of missing observations, the estimate using MMS and Mumford–Shah both provide a smooth temperature map. However, the estimated curves differ in the unobserved region. With Mumford–Shah, the estimated curve is almost a straight line across the missing observations. This occurs because the primary force in this region is due to the curve length penalty. However, with MMS, the curve exhibits characteristics more similar to the true boundary seen in Fig. 7(a). More importantly, the MMS result demonstrates that the estimate is consistent with the prior model on the field (i.e., the piecewise linear

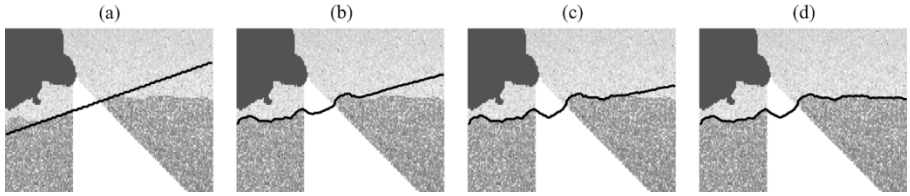

Fig. 9. Demonstration of curve evolution using the MMS functional. (a) The initial boundary, which is a straight line overlaid on the measurement data. (b) An intermediate step in the evolution. (c) A later intermediate step in the evolution. (d) Final boundary in the curve evolution process.

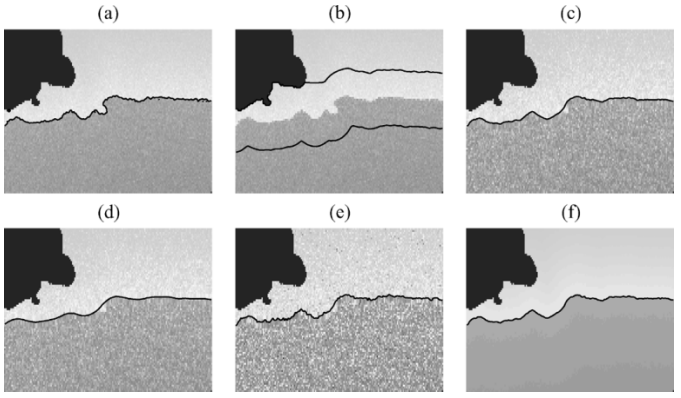

Fig. 10. Sensitivity analysis for initializations and parameter choice. (a) The field and boundary estimate of Fig. 7 using $\alpha = 0.7$, $\beta = 0.8$, and $\gamma = 8$. (b) Graph which shows band of possible initializations which result in the estimate in (a). (c) Result when the curve length parameter γ is set to 16. (d) Result when the curve length parameter γ is set to 40. (e) Result when the data fidelity parameter α is set to 7. (f) Result when the smoothness parameter β is set to 8.

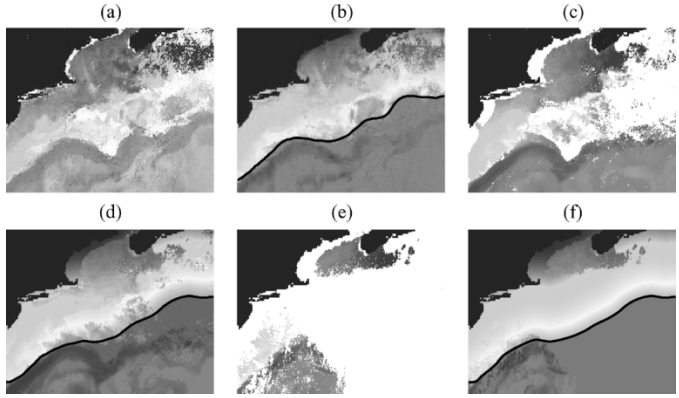

Fig. 11. Satellite SST estimation using MMS on GOES data with missing observations (white regions) due to cloud cover. (a) A satellite SST measurement with relatively few missing observations. (b) Field and boundary estimate based on measurements in (a). (c) A different SST map with more missing regions in the measurements. (d) Field and boundary estimate based on the measurements in (c). (e) A third SST map with most of the measurement information missing. (f) Field and boundary estimate based on (e).

mean assumption). In particular, the use of this prior model results in an upward concave curve where no measurements are present because the observations away from the boundary in the triangular region help determine its shape in MMS.

Quantitatively, Mumford–Shah yields a standard error of 0.76 degrees per pixel (1.36 in the triangular region), while MMS has a standard error of 0.73 per pixel (1.15 in the triangular region). Based on these results, we determine that the main difference is an improved boundary estimate in the unobserved area. Table III shows the standard error exhibited by each method within the unobserved triangular region.

To illustrate the functional minimization process, Fig. 9 shows four steps of the curve evolution process from an initial boundary [Fig. 9(a)], across two intermediate steps [first Fig. 9(b) and then Fig. 9(c)], and the final boundary estimate [Fig. 9(d)]. The boundary in each case is overlaid on the synthetic data.

To determine the robustness of the results, we provide some sensitivity analysis on the initializations and the choice of parameters. Using the simulated measurements shown in Fig. 7(b), we provide some analysis of how the results change with a corresponding change in parameter or initialization. Fig. 10(a) shows the result previously shown in Fig. 7(c). For this example, the parameters used are $\alpha = 0.7$, $\beta = 0.8$, and $\gamma = 8$. Regarding sensitivity to initializations, we randomly choose 40 smooth initial curves which extend from the left edge of the image to the right edge [one example of which is the initialization shown in Fig. 9(a)] which lie within the two bands shown in Fig. 10(b). For each of these initializations, the algorithm converges to an estimate that is visibly indistinguishable from the one shown in Fig. 10(a). Such a result indicates that the method is reasonably robust to different initializations of the boundary. Next, we examine the effect of increasing γ while leaving the other parameters fixed. Increasing γ first to 16 [Fig. 10(c)] and then to 40 [Fig. 10(d)] results in a progressive smoothing of the boundary as expected. Resetting γ back to 8 and setting α to 7 results in Fig. 10(e). Note that the result is noisier than Fig. 10(a) because it adheres more strongly to the observations. Finally, having $\alpha = 0.7$ and $\gamma = 8$, we set β to 8, resulting in a smooth field estimate as shown in Fig. 10(f).

2) Satellite SST Data: To demonstrate MMS on real data, we apply this functional to satellite SST data. In particular, we consider satellite images of the North Atlantic Ocean. Fig. 11(a) is a satellite image which shows a SST map having very little missing data. In this image, the dark mass in the upper left is land, the white regions represent missing observations, the blue regions are regions of cool water, and the orange and red regions are regions of warmer water. A temperature discontinuity exists at the Gulf Stream's north wall, as seen by the sharp separation of cooler waters in the north from the warmer waters in the south in Fig. 11(a). The satellite data are obtained from the National Oceanic and Atmospheric Administration (NOAA) Geostationary Operational Environment Satellite (GOES), courtesy of the Jet Propulsion Laboratory (JPL). The data are preprocessed using radiance measurement calibrations as described at the GOES web site (http://goes.gsfc.nasa.gov). Furthermore, recent works [83], [84] detail reasons (e.g., blackbody contamination) for calibration and analyze the radiometer calibration process. For this set of data, the means were chosen

to be linear functions of the distance from the curve, with the parameters determined empirically from examining historical sea surface temperature data of the North Atlantic. In particular, the mean temperature south of the Gulf Stream's north wall is assumed to be $\phi_1(d(\mathbf{x},\vec{C})) = 24.17 + 0.01d(\mathbf{x},\vec{C})$ degrees Celsius, where $d(\mathbf{x})$ is the distance in kilometers of the point $\mathbf{x}$ from the front. Similarly, the mean temperature north of the discontinuity is modeled as $\phi_2(d(\mathbf{x},\vec{C})) = 19.22 - 0.014d(\mathbf{x},\vec{C})$ degrees Celsius.

The covariance matrix was chosen to be the same as that used in the previous synthetic data example ($K[\mathbf{x},\mathbf{z}] = \exp[-0.02d^2(\mathbf{x},\mathbf{z})]$). A Gaussian covariance is a common model for field covariance within geophysical applications [12]. Fig. 11(a) shows a satellite SST image on a particular day where there is only a small percentage of missing observations due to cloud cover. By applying the MMS functional, the field estimate and boundary are shown in Fig. 11(b). For this example, the previous day's boundary was used as an initial estimate for the curve. The knowledge that the north wall of the Gulf Stream does not vary much from day to day is incorporated here to provide us with a good initialization for the curve $\vec{C}$. Having a good initialization generally leads to faster convergence during curve evolution.

In the previous example, the amount of missing observations was small. In some cases, a large portion of the region of interest may be unobserved. In these cases, the prior knowledge of the means and covariance plays a larger role in both the interpolation and boundary estimation. To illustrate, we consider SST maps for two different days which have larger areas which are unobserved [see Fig. 11(c) and Fig. 11(e)]. Whereas the image in Fig. 11(a) had 87% of the spatial domain visible, the observation in Fig. 11(c) has 66% data visible and the image in Fig. 11(e) has 19% data visible. Fig. 11(d) shows the boundary and field estimate based on observations from Fig. 11(c), while Fig. 11(f) shows the same given Fig. 11(e). In both of these examples, we have used the previous day's segmentation for the initial curve. Although we do not have access to the underlying truth in this experiment, we observe that the locations and shapes of the boundary estimates in all three examples are similar. Because the estimate based on 19% visible observations is similar to that based on 87%, we conclude that in the estimate shown in Fig. 11(f), the MMS functional does well in locating the boundary despite the sparsity of observations. In these two cases, the prior mean, coupled with observations far from the curve in the eastern portion of the North Atlantic, allows us to provide a reasonable estimate of the sea surface temperature in the unobserved regions. The field estimates also appear reasonable when compared to the field estimate in Fig. 11(b), an estimate made in the presence of most of the observations of that frame.

We now qualitatively examine the difference between the Mumford–Shah and MMS functionals on the GOES data. Fig. 12 provides a visual comparison of the field estimate using each functional based on the measurements shown in Fig. 12(a). Fig. 12(b) shows the field estimate using Mumford–Shah. Note that unlike the temperature estimate using MMS [Fig. 12(c)], the isotherms shown in Fig. 12(b) are not parallel to the oceanic front north of the Gulf Stream's north wall. The estimate bears this characteristic because Mumford–Shah smoothes across the unobserved region north of the boundary. In this particular example, the warm observations (shown in green and yellow) are in the western portion of the region while the cooler observations (blue) are in the eastern part of the region. Consequently, the temperature smoothing results in a west to east gradient. If we examine Fig. 11(a), we see that the region immediately north of the Gulf Stream's north wall is generally yellow in color. In Fig. 12(b), the region immediately north of the north wall in the eastern portion of the image is blue, indicating that the temperature has been underestimated. On the other hand, MMS has the physically more consistent field estimate which exhibits a south to north cooling as shown in Fig. 12(c), and is yellow in the region immediately north of the north wall. This is achieved because the MMS functional exploits each region's spatial statistics.

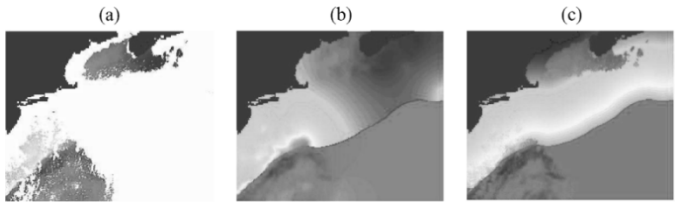

Fig. 12. Visual comparison of Mumford–Shah with MMS. (a) Observed data. (b) Field estimate of observed data using Mumford–Shah. (c) Field estimate using MMS.

VI. Conclusion

We have proposed methods of estimation and interpolation over a field having a discontinuity with unknown location and arbitrary shape. The two techniques we presented, Mumford–Shah and MMS, both solve a joint problem of boundary localization and field estimation. These two methods preserve discontinuities in the field. However, the benefit of our proposed MMS technique is that it allows for the incorporation of a variety of first- and second-order statistics. We have shown that certain estimation problems (e.g., SST estimation) yield improved results when the spatial statistics of the underlying field can be included in the functional formulation. Using sea surface temperature and simulated soil moisture data as examples, we have demonstrated the advantages of the proposed methods over three existing techniques of interpolation and smoothing that do not handle discontinuities.

The Mumford–Shah and MMS methods can be applied to other applications that: 1) have distinct regions in the data and 2) require interpolation given an incomplete or sparse set of measurements. One possible application is the estimation of hurricane or other severe weather damage. In such problems, given a data set of damage reports at a small set of locations, there is a desire to locate the boundary between regions of severe and less severe damage for determination of evacuation and protection of the affected region. Furthermore, insurance companies can use these methods to quickly obtain an estimate of the damage throughout the field. So, the techniques we have developed can be used to estimate the boundary as well as the surrounding field. Other earth science applications may have use for our techniques as well. In particular, we may want to locate the boundaries of the cusp-like structures of tropical instability waves near the equator from ocean color data [85], or locate rainstorms and estimate rainfall over a region using a combination of radar sensors [86].

The MMS functional can also be modified to incorporate dynamic information about the boundary when this information is available, especially when we are estimating the field and boundary over a temporal sequence. In particular, we can replace the curve length penalty term of (4) with a term that penalizes deviations of the current curve from a predicted curve. The predicted curve could, in principle, be obtained by taking past estimates of the boundary location, and evolving them according to the dynamics of the boundary. Having such a dynamic term in the functional can provide a more accurate prior model on the curves than a simple curve length penalty. This is a topic of our current research.

APPENDIX I
DERIVATION OF GRADIENT FLOW FOR THE MMS FUNCTIONAL

In Section IV-B, we discuss the steps taken to iteratively find the numerical solution of the problem. In this Appendix, we provide details regarding how the solution can be computed in discrete space. To do this, we must first write the MMS functional in discrete form. The third term in (4) discretizes to $(D(\mathbf{f}_{R_1} - \mathbf{m}_{R_1}))^T B_{R_1}(D(\mathbf{f}_{R_1} - \mathbf{m}_{R_1}))$, where D is a matrix approximation of the $\mathcal{D}$ operator, B_{R_1} is a matrix which represents the function b_{R_1}, and $\mathbf{f}_{R_1}$ and $\mathbf{m}_{R_1}$ are vectors representing the discretized version of f_{R_1} and μ_{R_1}, respectively. An equivalent form of this term is $(\mathbf{f}_{R_1} - \mathbf{m}_{R_1})^T D^T B_{R_1} D(\mathbf{f}_{R_1} - \mathbf{m}_{R_1})$. Similarly, the fourth term in (4) involving R_2 can be written as $(\mathbf{f}_{R_2} - \mathbf{m}_{R_2})^T D^T B_{R_2} D(\mathbf{f}_{R_2} - \mathbf{m}_{R_2})$. We can think of the term $D^T B_{R_i} D$ as an inverse covariance matrix ($K_{R_i}^{-1} \equiv D^T B_{R_i} D$); so, the discretized version of MMS can be written, with $\mathbf{f} = \begin{bmatrix}\mathbf{f}_{R_1}\\ \mathbf{f}_{R_2}\end{bmatrix}$, as

$$\begin{aligned} E\left(\begin{bmatrix}\mathbf{f}_{R_1}\\ \mathbf{f}_{R_2}\end{bmatrix}, \vec{C}\right) = \alpha\Big[\|H_{R_1}\mathbf{f}_{R_1} - \mathbf{g}_{R_1}\|_2^2 + \|H_{R_2}\mathbf{f}_{R_2} - \mathbf{g}_{R_2}\|_2^2\Big] \\ + \beta\Big[(\mathbf{f}_{R_1} - \mathbf{m}_{R_1})^T K_{R_1}^{-1}(\mathbf{f}_{R_1} - \mathbf{m}_{R_1}) \\ + (\mathbf{f}_{R_2} - \mathbf{m}_{R_2})^T K_{R_2}^{-1}(\mathbf{f}_{R_2} - \mathbf{m}_{R_2})\Big] \\ + \gamma l(\vec{C}) \end{aligned} \tag{8}$$

where the variables are defined as in (3). The choice of $\mathbf{f}_{\mathbf{R}_1}$ which minimizes (8) is

$$\begin{aligned} \mathbf{f}_{R_1} = K_{R_1} H_{R_1}^T \left(H_{R_1} K_{R_1} H_{R_1}^T + \frac{\beta}{\alpha} I\right)^{-1} \\ \times (\mathbf{g}_{R_1} - H_{R_1}\mathbf{m}_{R_1}) + \mathbf{m}_{R_1} \end{aligned} \tag{9}$$

where I is the identity matrix whose dimension is equal to the number of observations in the region. The result for $\mathbf{f}_{R_2}$ is similar to (9) with R_2 replacing every instance of R_1.

After solving for and updating $\mathbf{f}$ for a given curve $\vec{C}$, the next step is to evolve $\vec{C}$ with $\mathbf{f}$ fixed. We return to continuous space and derive the first variation of $E(f, \vec{C})$ with respect to $\vec{C}$ (the final result will be discretized for numerical implementation). The result provides us the direction of flow of $\vec{C}$ for which $E(f, \vec{C})$ decreases most rapidly. Known as the gradient flow for $\vec{C}$, it is often written as $\partial\vec{C}/\partial t$, or shorthand as $\vec{C}_t$, where t represents iteration time during the curve evolution step.

First, we write the MMS functional from (4) as

$$\begin{aligned} E(f, \vec{C}) = \alpha \int_{R_1(\vec{C}(t))\cap U} (f(\mathbf{x}) - g(\mathbf{x}))^2 \, d\mathbf{x} \\ + \alpha \int_{R_2(\vec{C}(t))\cap U} (f(\mathbf{x}) - g(\mathbf{x}))^2 \, d\mathbf{x} \\ + \beta\left(Q_{R_1(\vec{C}(t))}(t) + Q_{R_2(\vec{C}(t))}(t)\right) + \gamma \oint_{\vec{C}} ds. \end{aligned} \tag{10}$$

where $R_1(\vec{C}(t))$ and $R_2(\vec{C}(t))$ are the regions separated by $\vec{C}$,[6] $g(\mathbf{x})$ are the observations, U is the subset of Ω where observations of $g(\mathbf{x})$ exist, and Q is defined as

$$Q_{R(\vec{C}(t))}(t) = \int_{R(\vec{C}(t))} q_{R(\vec{C}(t))}(\mathbf{x}, t) d\mathbf{x} \tag{11}$$

with

$$q_{R(\vec{C}(t))}(\mathbf{x}, t) = \int_{R(\vec{C}(t))} v_R(\mathbf{x}, \mathbf{z}) d\mathbf{z} \tag{12}$$

where $v_R(\mathbf{x}, \mathbf{z}) = \mathcal{D}[f(\mathbf{x}) - \mu_R(\mathbf{x})] b_R(\mathbf{x}, \mathbf{z}) \mathcal{D}[f(\mathbf{z}) - \mu_R(\mathbf{z})]$. Note that since μ and b are fixed in this step, v_R does not depend on $\vec{C}(t)$. To find the curve evolution necessary to decrease $E(f, \vec{C})$, we compute the partial derivative of $E(f, \vec{C})$ with respect to t. Using the results derived by Kim *et al.* [87] and Delfour and Zolesio [88], we obtain

$$\begin{aligned} \frac{dQ_{R(\vec{C})}(t)}{dt} = \int_R \frac{\partial q_{R(\vec{C})}(\mathbf{x}, t)}{\partial t} d\mathbf{x} \\ + \oint_{\vec{C}} < q_{R(\vec{C})}(\mathbf{x}, t)\vec{N}, \vec{C}_t > ds \end{aligned} \tag{13}$$

and applying the result of Euclidean curve shortening $[(\partial/\partial t)\oint_{\vec{C}} ds = \oint < \vec{C}_t, \kappa\vec{N} > ds$, where κ is curvature] by Grayson [89], we obtain

$$\begin{aligned} \frac{\partial E\left(f, \vec{C}(t)\right)}{\partial t} = \alpha \oint_{\vec{C}(t)} \Big\langle \vec{C}_t, \Big(\Big(f_{R_2(\vec{C})}(s) - g(s)\Big)^2 \\ - \Big(f_{R_1(\vec{C})}(s) - g(s)\Big)^2\Big) h(s)\vec{N}\Big\rangle ds \\ + \beta \oint_{\vec{C}(t)} \Big\langle \vec{C}_t, \Big(q_{R_2(\vec{C}(t))}(s, t) \\ - q_{R_1(\vec{C}(t))}(s, t)\Big)\vec{N}\Big\rangle ds \end{aligned}$$

[6] In the body of the paper, we have used a shorthand notation to write these two terms as simply R_1 and R_2. Throughout this Appendix, we will be more explicit to make clear the dependencies of these regions on the curve.

$$+\beta\left[\int_{R_2(\vec{C}(t))}\frac{\partial q_{R_2(\vec{C}(t))}(\mathbf{x},t)}{\partial t}d\mathbf{x}-\int_{R_1(\vec{C}(t))}\frac{\partial q_{R_1(\vec{C}(t))}(\mathbf{x},t)}{\partial t}d\mathbf{x}\right]+\gamma\oint\langle\vec{C}_t,\kappa\vec{N}\rangle ds \tag{14}$$

where f_{R_i} represents the field estimate in R_i and $h(s)$ is an indicator function that takes the value of 1 when observations are present (i.e., when $s \in U$), and 0 otherwise. The negative signs arise from the fact that our outward normal $\vec{N}$ is taken with respect to R_1.

Since μ, and b are fixed, the integrand in (12) does not depend on $\vec{C}(t)$, but the region of integration does. In such a case, $(\partial q_{R(\vec{C}(t))}(\mathbf{x},t)/\partial t)$ can be written in the form of a line integral [90]. In particular,

$$\frac{\partial q_{R(\vec{C}(t))}(\mathbf{x},t)}{\partial t}=\frac{\partial}{\partial t}\int_{R(\vec{C}(t))}v_R(\mathbf{x},\mathbf{z})d\mathbf{z}=\int_{\vec{C}}\left\langle\vec{C}_t,v_R(\mathbf{x},s)\vec{N}\right\rangle ds. \tag{15}$$

Here, $\vec{N}$ represents the outward pointing normal vector with respect to region R.

Applying (15) to the two instances of $(\partial q_{R_i(\vec{C}(t))}(\mathbf{x},t)/\partial t)$ in (14), and assuming that b is symmetric (i.e., $b(\mathbf{x},\mathbf{z})=b(\mathbf{z},\mathbf{x})$, which implies $v(\mathbf{x},\mathbf{z})=v(\mathbf{z},\mathbf{x})$), we determine that

$$\left[\int_{R_2(\vec{C}(t))}\frac{\partial q_{R_2(\vec{C}(t))}(\mathbf{x},t)}{\partial t}d\mathbf{x}-\int_{R_1(\vec{C}(t))}\frac{\partial q_{R_1(\vec{C}(t))}(\mathbf{x},t)}{\partial t}d\mathbf{x}\right]=\oint_{\vec{C}(t)}\left\langle\vec{C}_t,\left(q_{R_2(\vec{C}(t))}(s,t)-q_{R_1(\vec{C}(t))}(s,t)\right)\vec{N}\right\rangle ds. \tag{16}$$

As a result, (14) simplifies to (17), shown at the bottom of the page. Now, the choice of $\vec{C}_t$ which yields the maximum decrease in $\langle\vec{C}_t,\epsilon\vec{N}\rangle$ is $\vec{C}_t=-\epsilon\vec{N}$. So, our flow equation, written in expanded form, is

$$\begin{aligned}\frac{\partial\vec{C}}{\partial t}(s)=&\alpha\left[\left(f_{R_2(\vec{C}(t))}(s)-g(s)\right)^2-\left(f_{R_1(\vec{C}(t))}(s)-g(s)\right)^2\right]h(s)\vec{N}\\&+2\beta\int_{R_2(\vec{C}(t))}\mathcal{D}\left[f(\mathbf{x})-\mu_{R_2(\vec{C}(t))}(\mathbf{x})\right]b_{R_2(\vec{C}(t))}(\mathbf{x},s)\\&\times\mathcal{D}\left[f(s)-\mu_{R_2(\vec{C}(t))}(s)\right]\vec{N}d\mathbf{x}\\&-2\beta\int_{R_1(\vec{C}(t))}\mathcal{D}\left[f(\mathbf{x})-\mu_{R_1(\vec{C}(t))}(\mathbf{x})\right]b_{R_1(\vec{C}(t))}(\mathbf{x},s)\\&\times\mathcal{D}\left[f(s)-\mu_{R_1(\vec{C}(t))}(s)\right]\vec{N}d\mathbf{x}\\&-\gamma\kappa(s)\vec{N}.\end{aligned} \tag{18}$$

For computational purposes, we desire a discrete version of (18). By defining D to be a matrix approximation of the $\mathcal{D}$ operator, B_{R_i} a matrix approximation of $b_{R_i}(\mathbf{x},\mathbf{z})$ (which we assume to be symmetric), diag[$\mathbf{w}$] to be a diagonal matrix with the vector elements of $\mathbf{w}$ along the main diagonal, and $\mathbf{f}$ and $\mathbf{m}$ as the vector representation of the discrete versions of f and μ, respectively, we obtain

$$\begin{aligned}\frac{\partial\vec{C}}{\partial t}(s)=\alpha&\left[\left(\left[H_{R_2}\mathbf{f}_{R_2}\right](s)-\mathbf{g}_{R_2}(s)\right)^2-\left(\left[H_{R_1}\mathbf{f}_{R_1}\right](s)-\mathbf{g}_{R_1}(s)\right)^2\right]\vec{N}\\&+2\beta\left(\left[\operatorname{diag}\left[D\left(\mathbf{f}_{R_2}-\mathbf{m}_{R_2}\right)\right]\times B_{R_2}\left(D\left(\mathbf{f}_{R_2}-\mathbf{m}_{R_2}\right)\right)\right](s)\right.\\&\left.-\left[\operatorname{diag}\left[D\left(\mathbf{f}_{R_1}-\mathbf{m}_{R_1}\right)\right]\times B_{R_1}\left(D\left(\mathbf{f}_{R_1}-\mathbf{m}_{R_1}\right)\right)\right](s)\right)\vec{N}-\gamma\kappa(s)\vec{N}\end{aligned} \tag{19}$$

where the index s to a vector refers to the element in that vector associated with the point s on the curve, t represents iteration time during the evolution of the active contour, $\kappa(s)$ is the curvature of $\vec{C}$ at s, diag[$\cdot$] is a diagonal matrix whose diagonal elements are given by the elements of the vector inside the square brackets, and $\vec{N}$ is the outward unit normal with respect to R_1. The numerical evolution is performed using level set methods [58], [59], and coordinate descent proceeds, alternating between updates of $\mathbf{f}$ and $\vec{C}$, until convergence.

$$\begin{aligned}\frac{\partial E\left(f,\vec{C}(t)\right)}{\partial t}=&\alpha\oint_{\vec{C}(t)}\left\langle\vec{C}_t,\left(\left(f_{R_2(\vec{C}(t))}(s)-g(s)\right)^2-\left(f_{R_1(\vec{C}(t))}(s)-g(s)\right)^2\right)h(s)\vec{N}\right\rangle ds\\&+2\beta\oint_{\vec{C}(t)}\left\langle\vec{C}_t,\left(q_{R_2(\vec{C}(t))}(s,t)-q_{R_1(\vec{C}(t))}(s,t)\right)\vec{N}\right\rangle ds-\gamma\oint\langle\vec{C}_t,\kappa\vec{N}\rangle ds\end{aligned} \tag{17}$$

A. Verification of Mumford–Shah Gradient Flow

Now, let us consider the special case where B_{R_i} is the identity matrix (in continuous space, this implies that $b_{R_i}(\mathbf{x},\mathbf{z})$ is the Dirac delta function). In this case, the curve flow can be simplified to

$$\begin{aligned}\frac{\partial \vec{C}}{\partial t}(s) = \alpha &\left[\left([H_{R_2}\mathbf{f}_{R_2}](s)-\mathbf{g}_{R_2}(s)\right)^2\right. \\ &\left.-\left([H_{R_1}\mathbf{f}_{R_1}](s)-\mathbf{g}_{R_1}(s)\right)^2\right]\vec{N} \\ &+2\beta\left[\left(D\left(\mathbf{f}_{R_2}-\mathbf{m}_{R_2}\right)\right)^2-\left(D\left(\mathbf{f}_{R_1}-\mathbf{m}_{R_1}\right)\right)^2\right](s)\vec{N} \\ &-\gamma\kappa(s)\vec{N}. \end{aligned} \tag{20}$$

We can further specialize to the case (in addition to B being the identity) by taking $\mathbf{m} = 0$ and $\mathcal{D}[\cdot]$ as the gradient operator. By making these choices, we simplify to the case of Mumford–Shah. In (14), we first observe that under these conditions, $q_{R_i(\vec{C}(t))}(\mathbf{x},t) = |\nabla f_{R_i}(\mathbf{x})|^2$ is not a function of t. So, the integrands of the region integrals (which contain time derivatives) are zero, reducing (14) to

$$\begin{aligned}\frac{\partial E\left(f,\vec{C}(t)\right)}{\partial t} = \alpha &\oint_{\vec{C}(t)} \left\langle \vec{C}_t, \left(\left(f_{R_2}(s)-g(s)\right)^2\right.\right. \\ &\left.\left.-\left(f_{R_1}(s)-g(s)\right)^2\right)h(s)\vec{N}\right\rangle ds \\ &+\beta\oint_{\vec{C}(t)}\left\langle \vec{C}_t, \left(|\nabla f_{R_2}(s)|^2-|\nabla f_{R_1}(s)|^2\right)\vec{N}\right\rangle ds \\ &+\gamma\oint\langle\vec{C}_t,\kappa\vec{N}\rangle ds. \end{aligned} \tag{21}$$

The curve flow obtained from (21) in discrete form is

$$\begin{aligned}\frac{\partial \vec{C}}{\partial t}(s) = \alpha &\left[\left([H_{R_2}\mathbf{f}_{R_2}](s)-\mathbf{g}_{R_2}(s)\right)^2\right. \\ &\left.-\left([H_{R_1}\mathbf{f}_{R_1}](s)-\mathbf{g}_{R_1}(s)\right)^2\right]\vec{N} \\ &+\beta\left[|\nabla\mathbf{f}_{R_2}(s)|^2-|\nabla\mathbf{f}_{R_1}(s)|^2\right]\vec{N}-\gamma\kappa(s)\vec{N} \end{aligned} \tag{22}$$

which is exactly the curve flow of Mumford–Shah as derived by Tsai [69].

B. Convergence of Gradient Flow

In Section IV-B, we mention that coordinate descent does not guarantee convergence to the global minimum. Consequently, the results may be sensitive to the choice of initialization. If several different initializations converge to different local minima, the desired field and boundary estimate should be the $(f,\vec{C})$ pair which results in the smallest functional value.

REFERENCES

[1] D. G. Krige, "A statistical approach to some basic mine valuation problems on the Witwaterstrand," *J. Chem., Metallurg. Mining Soc. South Afr.*, vol. 52, pp. 119–139, 1951.

[2] G. Matheron, "Principles of geostatistics," *Econ. Geol.*, vol. 58, pp. 1246–1266, 1963.

[3] P. Delfiner and J. P. Delhomme, "Optimum interpolation by kriging," in *Display and Analysis of Spatial Data*, J. D. Davis and M. J. McCullagh, Eds. New York: Wiley, 1975, pp. 96–114.

[4] I. Clark, *Practical Geostatistics*. London, U.K.: Applied Science, 1979.

[5] J. C. Davis, *Statistics and Data Analysis in Geology*. New York: Wiley, 1986.

[6] N. Cressie, *Statistics for Spatial Data*. New York: Wiley, 1991.

[7] A. Eliassen, "Provisional report on calculation of spatial covariance and autocorrelation of the pressure field," Inst. Weather and Clim. Res., Acad. Sci., Oslo, Tech. Rep. 5, 1954.

[8] L. S. Gandin, "Objective analysis of meteorological fields," Israel Program for Sci. Transl., Jerusalem, 1963. Translated from Russian.

[9] F. E. Bretherton, R. E. Davis, and C. B. Fandry, "A technique for objective analysis and design of oceanographic experiments applied to MODE-73," *Deep Sea Res.*, vol. 23, pp. 559–582, 1976.

[10] A. G. Journel and C. J. Huijbregts, *Mining Geostatistics*. Caldwell, NJ: Blackburn, 1978.

[11] H. J. Thiébaux and M. A. Pedder, *Spatial Objective Analysis: With Applications in Atmospheric Science*. London, U.K.: Academic, 1987.

[12] R. Daley, *Atmospheric Data Analysis*. Cambridge, U.K.: Cambridge Univ. Press, 1991.

[13] A. J. Mariano and O. B. Brown, "Efficient objective analysis of dynamically heterogeneous and nonstationary fields via the parameter matrix," *Deep Sea Res.*, vol. 39, pp. 1255–1271, 1992.

[14] W. S. Cleveland and C. Loader, "Smoothing by local regression: Principles and methods," in *Statistical Theory and Computational Aspects of Smoothing*, W. Haerdle and M. G. Schimek, Eds. New York: Springer-Verlag, 1996, pp. 10–49.

[15] G. Wahba and J. Wendelberger, "Some new mathematical methods for variational objective analysis using splines and cross validation," *Mon. Weather Rev.*, vol. 108, pp. 1122–1143, 1980.

[16] W. C. Thacker, "Fitting models to inadequate data by enforcing spatial and temporal smoothness," *J. Geophys. Res.—Oceans*, vol. 93, no. C9, pp. 10 655–10 665, 1988.

[17] J. Stephenson, K. Gallagher, and C. C. Holmes, "Beyond kriging: Daling with discontinuous spatial data fields using adaptive prior information and Bayesian prtition mdeling," in *Geological Prior Information*, A. Curtis and R. Wood, Eds. London, U.K.: Geol. Soc. London, 2005, pp. 1–33.

[18] I. Fukumori and P. Malanotte-Rizzoli, "An approximate Kalman filter for ocean data assimilation: An example with an idealized Gulf Stream model," *J. Geophys. Res.*, vol. 100, no. C4, pp. 6777–6793, 1995.

[19] A. R. Robinson, M. A. Spall, and N. Pinardi, "Gulf Stream simulations and the dynamics of ring and meander processes," *J. Phys. Oceanogr.*, vol. 18, pp. 1811–1853, 1988.

[20] L. J. Pratt, J. Earles, P. Cornillon, and J. F. Cayula, "The nonlinear behavior of varicose disturbances in a simple model of the Gulf Stream," *Deep Sea Res.*, vol. 38, pp. S591–S622, 1991.

[21] G. Podesta, J. Browder, and J. Hoey, "Exploring the association between swordfish catch rates and thermal fronts in the western North Atlantic," *Continent. Shelf Res.*, vol. 13, pp. 253–277, 1993.

[22] J. Cayula and P. Cornillon, "Multi-image edge detection for SST images," *J. Atmos. Oceanic Technol.*, vol. 12, pp. 821–829, 1995.

[23] P. Malanotte-Rizzoli and R. E. Young, "Gulf Stream system assimilation experiments: A sensitivity study," *J. Atmos. Oceanic Technol.*, vol. 14, no. 6, pp. 1392–1408, 1995.

[24] C. R. Williams, J. L. Bamber, A. Wilmshurst, N. Stapleton, and J. Scott, "Detection and tracking of oceanic thermal boundaries using passive microwave data," in *Proc. IGARSS*, vol. 3, 2000, pp. 1092–1094.

[25] A. Gangopadhyay and A. R. Robinson, "Feature-oriented regional modeling of oceanic fronts," *Dynam. Atmos. Oceans*, vol. 36, no. 1–3, pp. 201–232, 2002.

[26] T. J. Goreau and R. L. Hayes, "Coral bleaching and ocean "hot spots" ," *Ambio*, vol. 23, pp. 176–180, 1994.

[27] M. Buehner and P. Malanotte-Rizzoli, "Reduced-rank Kalman filters applied to an idealized model of the wind-driven ocean circulation," *J. Geophys. Res.*, vol. 108, no. C6, pp. 23-1–23-15, 2003.

[28] S. A. Margulis, D. McLaughlin, D. Entekhabi, and S. Dunne, "Land data assimilation and estimation of soil moisture using measurements from the Southern Great Plains 1997 field experiment," *Water Resources Res.*, vol. 38, no. 12, pp. 1–18, 1999.

[29] R. N. Atlas, N. Wolfson, and J. Terry, "The effects of SST and soil moisture anomalies on GLA model simulations of the 1988 US summer drought," *J. Climatol.*, vol. 6, no. 11, pp. 2034–2048, 1993.

[30] E. F. Lambin, "Modeling and monitoring land-cover changes processes in tropical regions," *Progr. Phys. Geograph.*, vol. 21, pp. 375–393, 1997.

[31] M. J. Fennessy and J. Shukla, "Impact of initial soil wetness on seasonal atmospheric prediction," *J. Climatol.*, vol. 12, no. 11, pp. 3167–3180, 1999.

[32] W. A. Gallus and M. Segal, "Sensitivity of forecast rainfall in Texas convective systems to soil moisture and convective parameterizations," *Weather Forecast.*, vol. 15, pp. 509–525, 2000.

[33] W. Wu, E. F. Lambin, and M.-F. Courel, "Land use and cover change detection and modeling for North Ningxia, China," in *Proc. Map Asia*, 2002.

[34] A. P. Burrough, "Multiscale sources of spatial variation in soil, I. The application of fractal concepts to nested levels of soil variation," *J. Soil Sci.*, vol. 34, no. 3, pp. 577–597, 1983.

[35] J. S. Famiglietti, J. A. Devereux, C. A. Laymon, T. Tsegaye, P. R. Houser, T. J. Jackson, S. T. Graham, and M. Rodell, "Ground-based investigation of soil moisture variability within remote sensing footprints during the Southern Great Plains 1997 (SGP97) Hydrology Experiment," *Water Resources Res.*, vol. 35, no. 6, pp. 1839–1851, 1999.

[36] B. P. Mohanty and T. H. Skaggs, "Spatio-temporal evolution and time-stable characteristics of soil moisture within remote sensing footprints with varying soil, slope, and vegetation," *Adv. Water Res.*, vol. 24, no. 9–10, pp. 1051–1067, 2001.

[37] J. M. H. Barton, S. G. Buchberger, and M. J. Lange, "Estimation of error and compliance in surveys by kriging," *J. Surv. Eng.*, vol. 6, no. 6, pp. 498–505, 2001.

[38] T. Ma, M. Sohpocleous, and Y. Yu, "Geostatistical applications in ground-water modeling in south-central Kansas," *J. Hydrol. Eng.*, vol. 4, no. 1, pp. 57–64, 1999.

[39] D. Thattai and S. Islam, "Spatial analysis of remotely sensed soil moisture data," *J. Hydrol. Eng.*, vol. 5, no. 4, pp. 386–392, 2000.

[40] C. C. Balascio, "Multiquadric equations and optimal areal rainfall estimation," *J. Hydrol. Eng.*, vol. 6, no. 6, pp. 498–505, 2001.

[41] R. E. Kalman, "A new approach to linear filtering and prediction problems," *Trans. Amer. Soc. Mech. Eng.*, ser. D, vol. 82, pp. 35–45, 1960.

[42] R. J. Meinhold and N. D. Singpurwalla, "Understanding the Kalman filter," *Amer. Statist.*, vol. 37, pp. 123–127, 1983.

[43] J. K. Yamamoto, "An alternative measure of the reliability of ordinary kriging estimates," *Math. Geol.*, vol. 32, no. 4, pp. 489–509, 2000.

[44] T. M. Chin, A. C. Haza, and A. Mariano, "A reduced-order information filter for multilayer shallow-water models: Profiling and assimilation of sea surface height," *J. Atmos. Oceanic Technol.*, vol. 19, no. 4, pp. 517–533, 2002.

[45] D. G. T. Denison, N. M. Adams, C. C. Holmes, and D. J. Hand, "Bayesian partition modeling," *Comput. Statist. Data Anal.*, vol. 38, pp. 475–485, 2002.

[46] D. Mumford and J. Shah, "Optimal approximations by piecewise smooth functions and associated variational-problems," *Commun. Pure Appl. Math.*, vol. 42, no. 5, pp. 577–685, 1989.

[47] ——, "Boundary detection by minimizing functionals I," in *Proc. IEEE Conf. Computer Vision and Pattern Recognition*, 1985.

[48] M. Kass, A. Witkin, and D. Terzopoulos, "Snakes: Active contour models," *Int. J. Comput. Vis.*, vol. 1, pp. 321–331, 1988.

[49] V. Caselles, F. Catte, T. Coll, and F. Dibos, "A geometric model for active contours in image processing," *Num. Math.*, vol. 66, pp. 1–31, 1993.

[50] Y. Chen, H. D. Tagare, S. Thiruvenkadam, F. Huang, D. Wilson, K. S. Gopinath, R. W. Briggs, and E. A. Geiser, "Using prior shapes in geometric active contours in a variational framework," *Int. J. Comput. Vis.*, vol. 50, no. 3, pp. 315–328, 2002.

[51] G. Kuhne, J. Weickert, O. Schuster, and S. Richter, "A tensor-driven active contour model for moving object segmentation," in *Proc. 2001 IEEE Int. Conf. Image Processing*, vol. 2, 2001, pp. 73–76.

[52] M. Leventon, E. Grimson, and O. Faugeras, "Statistical shape influence in geodesic active contours," in *Proc. IEEE Conf. Computer Vision Pattern Recognition*, vol. 1, 2000, pp. 158–175.

[53] N. Paragios and R. Deriche, "Geodesic active regions for texture segmentation. INRIA Tech. Rep.," INRIA, Rocquencourt , France, vol. 3440, 1998.

[54] ——, "Geodesic active contours and level sets for the detection and tracking of moving objects," *IEEE Trans. Pattern Anal. Mach. Intell.*, vol. 22, no. 11, pp. 266–280, Nov. 2000.

[55] T. M. Chin and A. Mariano, "Space-time interpolation of oceanic fronts," *IEEE Trans. Geosci. Remote Sens.*, vol. 35, no. 3, pp. 734–746, May 1997.

[56] J. A. Sethian, "Curvature and the evolution of fronts," *Commun. Math. Phys.*, vol. 101, pp. 487–499, 1985.

[57] A. Tsai, "Curve evolution and estimation-theoretic techniques for image processing," Ph.D. dissertation, MIT, Cambridge, MA, Aug. 2000.

[58] S. Osher and J. A. Sethian, "Fronts propagating with curvature dependent speed: Algorithms based on Hamilton–Jacobi formulation," *J. Comput. Phys.*, vol. 79, pp. 12–49, 1988.

[59] J. A. Sethian, *Level Set Methods: Evolving Interfaces in Geometry, Fluid Mechanics, Computer Vision, and Material Science*. Cambridge, U.K.: Cambridge Univ. Press, 1996.

[60] A. Blake and A. Zisserman, *Visual Reconstruction*. Cambridge, MA: MIT Press, 1987.

[61] G. Wahba, *Splines Models for Observational Data*. Philadelphia, PA: SIAM, 1990.

[62] D. Allen, "The relationship between variable selection and data augmentation and a method for prediction," *Technometrics*, vol. 16, pp. 125–127, 1974.

[63] G. Wahba and S. Wold, "A completely automatic French curve," *Commun. Statist.*, vol. 4, pp. 1–17, 1975.

[64] P. Craven and G. Wahba, "Smoothing noisy data with spline functions: Estimating the correct degree of smoothing by the method of generalized cross-validation," *Num. Math.*, vol. 31, pp. 377–403, 1979.

[65] P. C. Hansen, "Regularization tools: A MATLAB package for analysis and solution of discrete ill-posed problems," *Num. Alg.*, vol. 6, pp. 1–35, 1994.

[66] W. C. Karl, "Regularization in image restoration and reconstruction," in *Handbook of Image and Video Processing*. San Diego, CA: Academic, 2000.

[67] V. A. Morozov, "On the solution of functional equations by the method of regularization," *Sov. Math. Dokl.*, vol. 7, pp. 414–417, 1966.

[68] M. Leventon, "Statistical models in medical image analysis," Ph.D. dissertation, MIT, Cambridge, MA, May 2000.

[69] A. Tsai, J. A. Yezzi, and A. S. Willsky, "Curve evolution implementation of the Mumford–Shah functional for image segmentation, denoising, interpolation, and magnification," *IEEE Trans. Image Process.*, vol. 10, no. 8, pp. 1169–1186, Aug. 2001.

[70] T. F. Chan and L. A. Vese, "Active contours without edges," *IEEE Trans. Image Process.*, vol. 10, no. 2, pp. 266–277, Feb. 2001.

[71] A. Yezzi, A. Tsai, and A. Willsky, "Medical image segmentation via coupled curve evolution equations with global constraints," in *Proc. IEEE Workshop on Biomedical Image Analysis*, 2000, pp. 12–19.

[72] G. Christakos, "On the problem of permissible covariance and variogram models," *Water Resources Res.*, vol. 20, pp. 251–265, 1984.

[73] R. O. Weber and P. Talkner, "Some remarks on spatial correlation function models," *Mon. Weather Rev.*, vol. 121, pp. 2611–2617, 1993.

[74] M. S. Handcock and M. L. Stein, "A bayesian-analysis of kriging," *Technometrics*, vol. 35, pp. 403–410, 1993.

[75] L. P. Riishøjgaard, "A direct way of specifying flow-dependent background error correlations for meteorological analysis systems," *Tellus*, vol. 50A, pp. 42–57, 1998.

[76] G. Gaspari and S. E. Cohn, "Construction of correlation functions in two and three dimensions," *Q. J. R. Meteorol. Soc.*, vol. 125, pp. 723–757, 1999.

[77] D. McLaughlin, "Environmental data assimilation: Methods and challenges," in *Proc. 15th Int. Conf. Computational Methods in Water Resources, Pt 2*, vol. 55, 2004, pp. 1–15.

[78] G. B. Bonan, K. W. Oleson, M. Vertenstein, and S. Levis, "The land surface climatology of the community land model coupled to the NCAR community climate model," *J. Clim.*, vol. 15, no. 22, pp. 3123–3149, 2002.

[79] Y. Zhou and D. McLaughlin, "Optimality assessment of the ensemble Kalman filter for land surface data assimilation," *Water Resource Manage.*, 2005, submitted for publication.

[80] M. I. Budyko, "The effect of solar radiation on the climate of the Earth," *Tellus*, vol. 21, pp. 611–619, 1969.

[81] W. D. Sellers, "A global climatic model based on the energy balance of the Earth atmosphere system," *J. Appl. Meteorol.*, vol. 8, pp. 391–400, 1969.

[82] A. Papoulis, *Probability, Random Variables, and Stochastic Processes*. New York: McGraw-Hill, 1991.

[83] J. W. Brown and R. H. Evans, "Calibration of AVHRR infrared channels: A new approach to nonlinear correction," *J. Geophys. Res.*, vol. 98, no. 18, pp. 257–268, 1993.

[84] A. P. Trishchenko and Z. Li, "A method for the correction of AVHRR onboard IR calibration in the event of short-term radiative contamination," *Int. J. Remote Sens.*, vol. 22, no. 17, pp. 3619–3624, 2001.

[85] M. Jochum, P. Malanotte-Rizzoli, and A. Busalacchi, "Tropical instability waves in the Atlantic Ocean," *Ocean Model.*, vol. 1–2, no. 7, pp. 145–163, 2004.

[86] I. P. Gorenburg, D. McLaughlin, and D. Entekhabi, "Scale-recursive estimation of precipitation at the TOAGA-COARE site," *Adv. Water Res.*, vol. 24, pp. 941–953, 2001.
[87] J. Kim, J. W. Fisher, III, A. Yezzi, Jr., M. Cetin, and A. S. Willsky, "Nonparametric methods for image segmentation using information theory and curve evolution," in *Proc. IEEE Conf. Image Processing*, vol. 3, Rochester, NY, Sep. 2002, pp. 797–800.
[88] M. C. Delfour and J. Zolesio, *Shapes and Geometries: Analysis, Differential Calculus, and Optimization*. Philadelphia, PA: SIAM, 2001.
[89] M. Grayson, "The heat equation shrinks embedded plane curves to round points," *J. Diff. Geom.*, vol. 26, pp. 285–314, 1987.
[90] A. Yezzi, A. Tsai, and A. Willsky, "Fully global, coupled curve evolution equations for image segmentation," MIT, Cambridge, MA, MIT LIDS Tech. Rep., 1999.

Walter Sun (S'94–M'03) received the B.S. degree from the Georgia Institute of Technology, Atlanta, and the M.S., E.E., and Ph.D. degrees from the Massachusetts Institute of Technology, Cambridge, in 1995, 1997, 2004, and 2005, respectively, all in electrical engineering.

He is an NDSEG Graduate Fellowship recipient. He is currently with Microsoft Corporation, Redmond, WA. His research interests include statistical signal and image processing, computer vision, stochastic finance, and image coding.

Müjdat Çetin (S'98–M'02) received the Ph.D. degree in electrical engineering from Boston University, Boston, MA, in 2001.

Since 2001, he has been a member of the Laboratory for Information and Decision Systems, Massachusetts Institute of Technology, Cambridge, where he now holds the title of Research Scientist. Since September 2005 he has also been an Assistant Professor at Sabanci University, Istanbul, Turkey. His research interests include statistical signal and image processing, inverse problems, computer vision, data fusion, wireless sensor networks, biomedical information processing, radar imaging, and sensor array signal processing.

Dr. Çetin has served in various organizational capacities, including Special Session Organizer, Session Chair, and Technical Program Committee Member for a number of conferences including the IEEE International Conference on Image Processing, the IEEE International Conference on Acoustics, Speech, and Signal Processing, the IEEE Statistical Signal Processing Workshop, the ACM Conference on Embedded Networked Sensor Systems, the SPIE Conference on Algorithms for Synthetic Aperture Radar Imagery, the EURASIP European Signal Processing Conference, and the IEEE Global Telecommunications Conference.

W. Carlisle Thacker received the B.S. degree in applied mathematics from the Georgia Institute of Technology, Atlanta, and the M.S. and Ph.D. degrees from the University of Illinois at Urbana-Champaign, in 1965, 1967, and 1971, respectively.

He is currently a Research Scientist at the Atlantic Oceanographic and Meteorological Laboratory, Miami, FL. His research interests include the assimilation of data into numerical models of oceanic circulation.

T. Mike Chin received the B.S. and M.S. degrees from the University of California, Berkeley, and the E.E. and Ph.D. degrees from the Massachusetts Institute of Technology, Cambridge, in 1982, 1983, 1990, and 1992, respectively, all in electrical engineering.

He was with the Computer Vision and Image Processing Laboratory, University of California, Davis, from 1984 to 1985, and with the National Center of Atmospheric Research, Boulder, CO, from 1994 to 1996, through the Advanced Study Program. He is currently a Research Scientist at the Jet Propulsion Laboratory, California Institute of Technology, Pasadena, with aso an appointment as a Research Associate Professor of physical oceanography at the University of Miami, Miami, FL.

Alan S. Willsky (S'70–M'73–SM'82–F'86) joined the faculty of the Massachusetts Institute of Technology, Cambridge, in 1973, and is currently the Edwin Sibley Webster Professor of Electrical Engineering. He was a founder, member of the Board of Directors, and Chief Scientific Consultant of Alphatech, Inc., and since its acquisition in November 2004 continues as Chief Scientific Consultant for BAE Systems Advanced Information Technologies. From 1998 to 2002, he served as a member of the U.S. Air Force Scientific Advisory Board. He has held visiting positions in the U.K. and France and various leadership positions in the IEEE Control Systems Society (which made him a Distinguished Member in 1988). He has delivered numerous keynote addresses and is coauthor of the undergraduate text *Signals and Systems* (2nd ed., Prentice-Hall, 1997). His research interests are in the development and application of advanced methods of estimation and statistical signal and image processing. Methods he has developed have been successfully applied in a variety of applications including failure detection, surveillance systems, biomedical signal and image processing, and remote sensing.

Dr. Willsky has received several awards including the 1975 American Automatic Control Council Donald P. Eckman Award, the 1979 ASCE Alfred Noble Prize, the 1980 IEEE Browder J. Thompson Memorial Award, the 2004 IEEE Donald G. Fink Prize Paper Award, and Doctorat Honoris Causa from Université de Rennes, France in 2005.